ACTIVE MAGNETIC BEARINGS
FOR LARGE VARIABLE HIGH-SPEED MOTORS

Paper No. PCIC Europe EUR26_22

Dr. Lionel Durantay
Senior Member, IEEE
GE Vernova PCS
442, rue de la Rompure
54250 Champigneulles
France
lionel.durantay@gevernova.com

Jules Marulier
GE Vernova PCS
442, rue de la Rompure
54250 Champigneulles
France
jules.marulier@gevernova.com

Lionel Broussard
GE Vernova PCS
15 Rue Jean Bart
91300 Massy
France
lionel.broussard@gevernova.com

Christophe Grosselin
GE Vernova PCS
442, rue de la Rompure
54250 Champigneulles
France
christophe.grosselin@ gevernova.com

Abstract – Due to the rise of electronics and controls during the 1960s, the first active magnetic levitation bearings were developed during the 1970s, a century and a half after the invention of mechanical bearings. Fifty years later, these bearings are experiencing a boom. The first part of this paper describes the operating principle of an electromagnet and compares, for large variable high-speed motors, the limiting factors of antifriction bearings, hydrodynamic bearings and active magnetic bearings. The second part details the components, the control principle of active magnetic bearings, their integration into an 8MW@15000rpm induction motor, and their advantages in terms of shaft line dynamics compared to oil bearings. The last part explains the rigid mode control of the motor with experimental measurements of the associated transfer functions and rotor orbits. The conclusion describes the technological coverage prospects of active magnetic bearings for high-speed, high-power electric machines up to 100 MW.

Index Terms – Active magnetic bearings, Control, Loop-shaping

I. INTRODUCTION – HOW TO MOVE PARTS?

Since prehistoric times, humanity has had to find solutions to move objects or make them rotate after the invention of the wheel. During antiquity, for the construction of the pyramids, Egyptian architects developed methods of ramps (Fig.1) allowing the blocks to be hoisted, and of moving loads with structures around the block (Fig.2) [1]. A few centuries later, roman chariots had a simple system to allow the wheels to turn quickly. The axle (or shaft) was a wooden bar fixed under the chariot. The wheels rotated around the axle, thanks to a reinforced central hole in the hub, which was fitted with a metal bushing to limit wear and lubricated with animal fat (Fig.3).

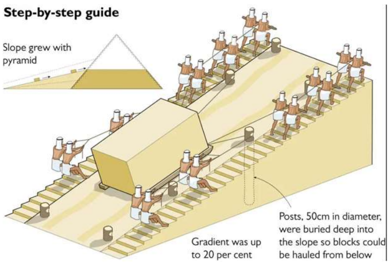

Figure 1 Egyptian method of ramp

Figure 2 Egyptian moving load

Around 1495, Leonardo da Vinci invented the first antifriction bearing with the idea of an axial thrust bearing with eight balls separated by rotors used to move a weight with wheels on axles that hold the balls in place so that they rotate and cannot escape (Fig.5) [2]. Over time, the lifespan of anti-friction bearings has been improved by reducing friction and wear with increasingly smaller manufacturing tolerances for parts, and with lubricants more resistant to high temperatures, moving from tallow to mineral grease, and from olive oil to mineral. Hydrodynamically lubricated plain bearings were invented in 1886 by Beauchamp Tower and Osborne Reynolds for railway axle bearings. Their experiments showed that a rotating shaft could be supported by a pressurized oil film generated by the motion (Fig.4). The shear constraints of the oil film determine the limits of use of these bearings in terms of tip speed and loads.

Figure 3 Roman chariot rolling system
(Saint-Raymond Museum)

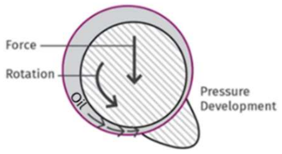

Figure 4 Hydrodynamic oil-lubricated sleeve bearing

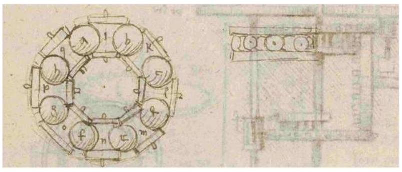

Figure 5 Ball thrust bearing with interposed rotors (1493-1497) by Leonardo Di Vinci

II. ACTIVE MAGNETIC BEARINGS FOR HIGH-SPEED ELECTRIC MOTORS

A. Active Magnetic Bearings

The next step was to eliminate contact and therefore friction between the fixed part and the shaft in the bearing. The concept of magnetic suspension has existed since the beginning of the 20th century. Active magnetic bearings (AMBs) were developed in the late 1970s in Switzerland by Gerhard Schweitzer and Eric H. Maslen for rotor suspension controlled and stabilized by feedback [3]. The electromagnet pulling force of the active magnetic bearing ($\mathrm{F_{pull}}$) is given as follow where (σ_{mag}) is the Maxwell magnetic pressure, ($\mathrm{g_x}$) is the airgap, (S) is the airgap area and ($\mathrm{B_{airgap}}$) is the airgap induction field (Fig.6):

$$\mathrm{F_{pull}} = (\sigma_{\mathrm{mag}}).\mathrm{S} = \left(\frac{\mathrm{B^2_{airgap}}}{2\,\mu_0}\right).\mathrm{S} \qquad (1)$$

$$B_{airgap} = \frac{\mu_0 * N * I}{2 * g_x} \tag{2}$$

The losses are mainly generated by Joule losses in the electromagnet's winding:

$$\text{Power Consumption} = R_a * I^2 \tag{3}$$

With an induction (B_{airgap}) of 0.8 Tesla in an airgap (g_x) of 1mm, the electromagnet levitates with a steel mass of 1 ton with a power of the order of 100 Watt (Table I):

TABLE I
ELECTROMAGNET ACTUATOR CHARACTERISTICS

Levitated Mass (m)	1000 kg
Airgap (g_x)	1 mm
Current (I)	30 A
Number of Turns (N)	42
Airgap Induction (B_{airgap})	0.8 T
Magnetic Pressure (σ_{mag})	0.25 N/mm²
Airgap Surface (S)	20000 mm²
Coil Resistance (R_a)	0.11 Ω
Power Consumption	≈ 100 W

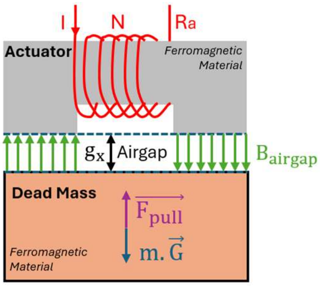

Figure 6 Electromagnetic actuator principle

The functioning of one axis (x) of a radial bearing is described by Fig. 6. An active magnetic bearing is constituted by a displacement sensor technology generally, inductive (variable reluctance or eddy current) in a Wheatstone bridge arrangement, that produces an electric signal (U_x) proportional to the rotor relative displacement (X). A controller then computes from this signal a command (U_I) intended for the actuator. This signal is transformed to a proportional current ($I^{(k)}$) in electromagnet coils which produces through the actuator (#k) a pulling force $\left(F_X^{(k)}\right)$ on the rotor:

$$F_X^{(k)} = \frac{4\mu_0 \,.\, S\cos(\alpha) \;\; .\, N^2 .\, I^{(k)\,2}}{\left(\frac{L_a}{\mu_r} + 2.\, g_X^{(k)}\right)^2} \tag{4}$$

where the impedance of the actuator is:

$$Z_{actuator} = R_a + j\, L_a \omega \tag{5}$$

The rotor of the actuator consists of a solid core and outer part made of laminated steel. The purpose of the lamination is to reduce the effects of eddy currents when the rotor is rotating and when the bearing forces are controlled. The stator of the actuator is made of laminated steel as well. The winding of an electromagnet is made of regular copper wire (Fig. 10). The design consists in sizing the induction in the ferromagnetic parts below saturation which helps for the linearization of this force. Up to half of the maximum current is used to withstand the static load (rotor mass) while the remainder is used to control the dynamic loads. Electromagnets can produce only magnetic attraction forces. Recall that with a constant current, a decrease in the air gap, increases the force. Consequently, the system is naturally unstable, since it aims to pull the rotor onto the bearing inner surface. In practice, two counteracting electromagnets, named #1 and #2 in the x direction, operating in differential driving mode are employed to control the rotor. When rotor is moving down with a motion (X), the airgaps of the actuators # 1 and #2 are respectively equal to:

$$g_X^{(1)} = g_0 - X \text{ and } g_X^{(2)} = g_0 + X \tag{6}$$

The control will generate with the amplifiers the unbalanced currents ($I^{(1)}$) and ($I^{(2)}$) of (I_x),, in the actuator stators # 1 and #2 to regulate the rotor position:

$$I^{(1)} = I_0 + I_X \text{ and } I^{(2)} = I_0 - I_X \tag{7}$$

The resulting force $\left(F_X^{(1,2)}\right)$ can be linearized:

$$F_X^{(1,2)} = F_X^{(1)}(I_0 + I_X\,, g_0 - X) - F_X^{(2)}(I_0 - I_X\,, g_0 + X) \tag{8}$$

$$F_X^{(1,2)} = K_I * I_X - K_X(\Omega,\omega) * X \tag{9}$$

$$\text{Where } K_I = \left(\frac{\partial F_X^{(1,2)}}{\partial I_X}\right)_{g_0, I_0} \tag{10}$$

$$\text{and } K_X(\Omega,\omega) = \left(\frac{\partial F_X^{(1,2)}}{\partial X}\right)_{g_0, I_0} \tag{11}$$

The input force seen by the rotor at the bearing's location is:

$$\text{Input Force (t)} = F(\omega)\,.\,e^{-j(\omega t+\delta)} + K_I * I(\omega)\,.\,e^{-j(\omega t+\beta)} \tag{12}$$

where $(F(\omega))$ is the dynamic excitation coming from the rotating and the static parts of the system caused by a periodic excitation, which consists of a finite number of harmonic components (ω).

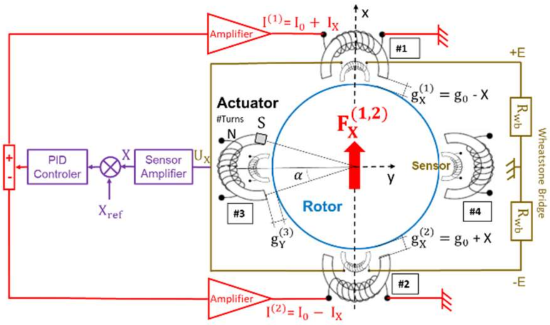

Figure 7 Active Magnetic Bearings control loop

The Complex Dynamic Stiffness (CDS) is defined by the ratio of the Input Force by the measured Output Displacement $(X(\omega))$:

$$\text{Output Displacement (t)} = X(\omega) * e^{-j\omega t} \tag{13}$$

$$\text{CDS} = \text{Input Force (t)} \,/\, \text{Output Displacement (t)} \tag{14}$$

The system stiffness ($K_{syst}\,(\Omega,\omega,\varphi)$) and damping ($C_{syst}\,(\Omega,\omega,\varphi)$), at the bearings location, vary as a function of disturbance pulsations (ω) and the rotor rotational speed (Ω) coming from:

- dynamic excitations: $F(\omega)$
- dynamic stiffness of static and rotating parts: $K - (M * \omega^2)$
- viscous damping of static parts D_s
- viscous damping of rotating parts D_r

These dynamic perturbations are counterbalanced by the controller transfer function through the filters controlling the AMB stiffness:

$$K_{AMB}\ (\Omega,\omega,\varphi) = K_x(\Omega,\omega)\ * \exp\,[j.(\,\varphi(\Omega,\omega)\,)] \tag{15}$$

which is piloted to meet the system dynamic requirement considered in the overall machine design (Table I):

$$CDS = K_{syst}\ (\Omega,\omega,\varphi) + j\ *\ C_{syst}\ (\Omega,\omega,\varphi) * \omega \tag{16}$$

$$K_{syst}\ (\Omega,\omega,\varphi) = K - M * \omega^2 + [\,K_x(\Omega,\omega)\ * \cos\varphi(\Omega,\omega)] \tag{17}$$

$$C_{syst}\ (\Omega,\omega,\varphi) = [D_s - D_r] + [\frac{K_x(\Omega,\omega)}{\omega} * \sin\varphi(\Omega,\omega)] \tag{18}$$

A closed loop control system can be implemented in a microprocessor-based controller to stabilize the rotor in its steady state position by piloting the voltage of the actuator through the following equations:

$$\text{AMB Voltage}\ (t) = U_{piloted}(\omega)\ *\ e^{-j(\omega t+\tau)} \tag{19}$$

$$U_{piloted}\ (\omega) = (R_a + j.L_a\omega) * I(\omega).e^{-j\beta} + j * h.\omega.X(\omega).e^{-j\varphi} \tag{20}$$

B. Large High-speed Motors equipped with AMB(s)

High speed motors have predefined power versus speed capability curves. The maximum allowable operating speed is related to the mechanical stresses defining the rotor diameter. The squirrel cage rotor is adapted for high-speed conditions and comprises a steel lamination assembly compressed by tie rods between two end rings and two shaft ends (Fig. 8). The cage bars can expand axially through the end ring. The copper bars are inserted in the slots between the two end rings to form the squirrel cage. The laminated technology allows high efficiency, and high rotor peripheral speed up to 270 m/s, not sensitive to thermal unbalance providing high robustness in terms of aging and stability over the time [4].

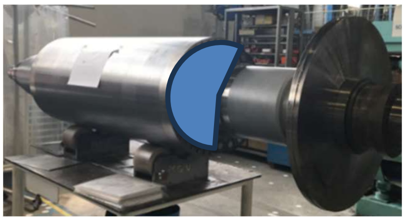

Figure 8 Laminated squirrel cage high-speed rotor with AMB bearings parts

The magnetic induction in the airgap of the radial active magnetic bearing (B_{airgap}) is of the order of 1.5 Tesla because of magnetic saturation in the laminations of the bearing (Fig.12), generating a magnetic pressure around 1 N/mm² and magnetic stiffness around 10^{-3} N/m. The stiffness of AMB is very soft compared to an oil film. Illustrated on a system operating at 7MW@13200rpm (Fig.9), compared to oil bearings, the magnetic bearings, because of their low stiffness control, avoid any modes in the operating speed range of the system. The stiffness of AMB is frequency controlled, with zero stiffness injection at the rotational frequency, the rotor spinning around its instantaneous center of inertia. This makes it possible to inject no unbalance force into the structures of the platform, avoiding possible resonances compared to an arrangement on oil bearings.

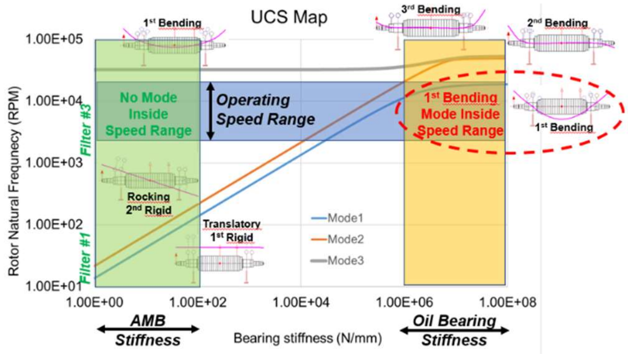

Figure 9 Undamped critical speed Map 6.9MW@13200rpm induction motor

In a system with active magnetic bearings, when the power supply is lost (including the UPS inside the cubicle) (Fig.11) or the control system fails, the rotor must be mechanically supported to prevent impact with the stator. This is where the backup bearings come into play. They provide mechanical protection for the shaft and electronics when the magnetic support is inactive. Advanced rolling elements are ceramic balls that reduce mass, improve wear resistance, and better withstand vibrations and impacts during rotor landing [5]. Although hard landings are very rare, the electric motor is designed so that the two landing bearings located at each end of the frame can be easily replaced (Fig.10). There is no maintenance to be done on the actuators which guarantees availability rates of over 99% for magnetic bearing systems and maintenance intervals of over 6 years.

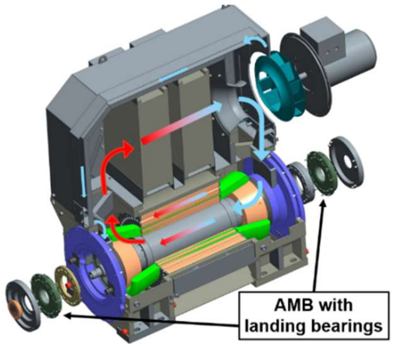

Figure 10 High-speed Induction Motor Cooling and AMB Design for Easy Maintenance

Figure 11 Cubicle & Motor

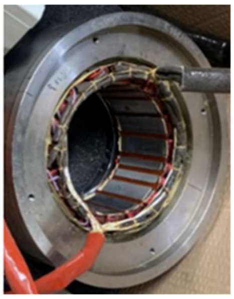

Figure 12 Stator Actuator

Typical radial magnetic bearing air gaps are 0.5mm. It eliminates the risk of capacitive discharges in the bearings due to the zero-sequence switching voltages of the 3-phase Voltage Source Inverter. This also allows for very good cooling of the static and rotating parts of the bearings with air or a process gas such as natural gas.

The main advantages of AMBs are listed below:

- No wear, no mechanical maintenance and unlimited lifetime, moreover, no bearing noise,
- 200 m/s bearing tip speed achievable,
- Very low friction losses of the gas,
- No process fluid contamination by the bearing
- No need for seal, oil lube system and accessories,
- Ability to work in vacuum or hostile environments,
- Permanent control of rotation axis,
- Automatic balancing system, rotor spinning around its inertial axis instead of its geometrical axis,
- Adapting static and dynamic stiffnesses for high accuracy of rotation,
- Vibration free control,
- Permanent monitoring of the system.
- Low risk of electric arching,
- Low energy consumption.

Active magnetic bearings, compared to antifriction or oil-lubricated hydrodynamic bearings, are the most efficient for high-power and variable-speed electrical machines (Table I):

TABLE II
BEARING TYPES COMPARISON
FOR LARGE HIGH-SPEED MACHINE

Bearing Type	Antifriction	Oil Sleeve	AMB
Rotor Tip Speed	< 80 m/s	< 150 m/s	< 250 m/s
Specific Load	< 5 MPa	< 15 MPa	< 0.5 MPa
Medium	Mineral Oil	Mineral Oil	Gaseous
Medium leakage	Possible	Possible	No
Gap/Film	< 10 µm	< 50 µm	< 1000 µm
Arcing Voltage	> 1 Volts	> 10 Volts	> 100 Volts
Electric Insulation	Yes	Yes	No
Heat Dissipation	< 10 W/mm²	< 1 W/mm²	< 0.1 W/mm²
Max admissible temperature	90°C	100°C	180°C stator 130°C rotor
Auxiliaries	Oil reservoir Oil mist device	Oil-Forced lubrication with pump	Power electronic cubicle
Auxiliaries Consumption	< 0.5 Oil Liters/min for 1 ton of rotor	< 3 Oil Liters/min for 1 ton of rotor	300 Watt for 1 ton of rotor
Friction Risk Mitigation	Track & Rolling elements hardening	White metal - Jacking unit Hydrostatic lifting device	Landing bearing - UPS
Maintenance	Oil cleaning Oil circuit Oil leakage	Oil cleaning Oil circuit Oil leakage Sleeve	Landing bearings Power Electronics
Lifetime	< 100 000 h	20 years +	25 years +

C. Loop-Shapping Control Method

The most complex part of active magnetic bearings is not the hardware and electrical components, but the control system (Fig.13). Current microprocessors allow sampling frequencies compatible with very high rotational speeds of several tens of thousands of revolutions per minute.

Loop shaping control is used for these applications. Loop shaping is a frequency-domain control design approach in which the controller is built to shape the open-loop transfer function of the system to achieve desired closed-loop performance and robustness. The main idea is to modify the loop gain over specific frequency ranges so that stability margins, disturbance rejection, and noise attenuation requirements are simultaneously satisfied. The design process typically starts from a linearized model of the plant and focuses on the open-loop transfer function:

$$L(s) = G(s) * K(s) \tag{21}$$

where G(s) is the plant dynamics and K(s) is the controller.

By shaping the magnitude and phase of L(s), the designer directly influences key closed-loop properties such as bandwidth, sensitivity to disturbances, and robustness to modeling uncertainties.

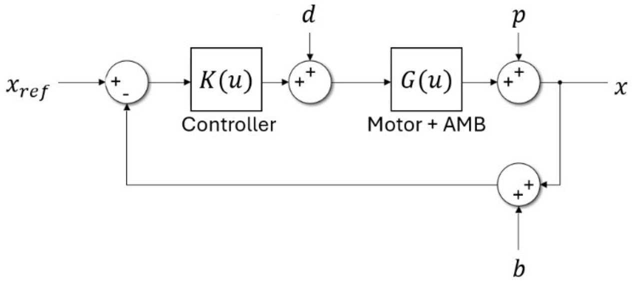

Figure 13 Closed loop System

At low frequencies, high loop gain is imposed to ensure accurate reference tracking and effective rejection of low-frequency disturbances, such as static loads or rotor imbalance forces in active magnetic bearing systems. In the mid-frequency range, the loop is shaped to achieve sufficient phase margin, which guarantees closed-loop stability and acceptable transient response. At high frequencies, the loop gain is reduced to limit noise amplification and to account for unmodeled high-frequency dynamics and actuator limitations. Loop shaping naturally provides robustness by enforcing adequate gain and phase margins, and it offers an intuitive design framework based on frequency-domain insight.

It is particularly well suited for active magnetic bearing systems, where open-loop instability, model uncertainties, and bandwidth constraints must be carefully balanced. The resulting controller is often implemented using classical structures, such as lead-lag compensators or PID-based architectures, possibly augmented with filters to address specific resonance or noise issues. Instead of controlling rotor motion independently in Cartesian coordinates, modal control expresses the rotor dynamics in terms of cylindrical (Fig.14) and conical modes (Fig.15). The cylindrical mode represents a rigid-body translation of the rotor, where both bearings move in phase, while the conical mode corresponds to a tilting motion, with opposite-phase displacements at the bearings. This modal transformation allows an approximate decoupling of the system dynamics, leading to independent control of each mode. As a result, controller parameters can be tuned according to the specific dynamic characteristics of the cylindrical and conical modes, which typically exhibit different natural frequencies and damping requirements. Compared to Cartesian control, modal control improves physical interpretability, reduces cross-coupling effects, and facilitates targeted damping of critical rotor dynamics.

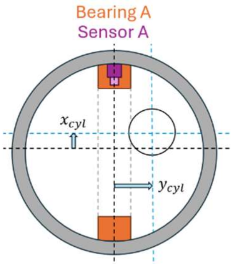

Figure 14 Rotor Cylindrical Mode

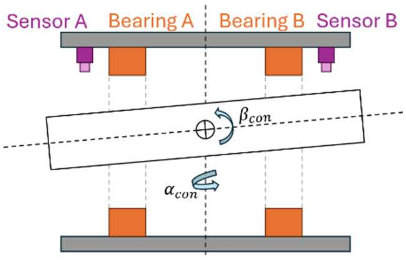

Figure 15 Rotor Conical Mode

The modal control actions are finally transformed back into Cartesian actuator commands, ensuring compatibility with standard sensor and actuator configurations. These two controllers are constructed with:

- an integral term

$$\frac{K_{Ic}}{s} \tag{22}$$

- a third-order phase-lead compensator

$$K_{Dc}\left(\frac{T_p + 1}{\alpha_D\, T_p\, s + 1}\right)^3 \tag{23}$$

- a low-pass filter of the form

$$\frac{1}{\beta_D\, T_p\, s + 1} \quad \text{or} \quad \frac{1}{\left(\frac{s^2}{\omega_0^2} + 2\frac{\xi}{\omega_0} s + 1\right)} \tag{24}$$

- and a set of notch filters denoted

$$F_{No}(s) = \frac{1 - 2\frac{\xi_{No}}{\omega_n} s + \frac{s^2}{\omega_n^2}}{1 + 2\frac{\xi_{No}}{\omega_n} s + \frac{s^2}{\omega_n^2}} \tag{25}$$

The controller is structured as an integral action followed by a third-order phase-lead compensator and a low-pass filter to simultaneously ensure stability, performance, and robustness of the closed-loop system. The integral action is introduced to guarantee zero steady-state error and to provide high loop gain at low frequencies. This is particularly important in active magnetic bearing systems, where constant disturbances such as static loads, rotor weight, or imbalance forces must be effectively rejected. The integrator ensures accurate positioning of the rotor around its equilibrium point. The third-order phase-lead compensator is used to increase the phase margin and to extend the achievable closed-loop bandwidth. Due to the intrinsic open-loop instability and lightly damped dynamics of magnetic bearing systems, a significant phase boost is required around the crossover frequency. Using a higher-order phase-lead structure allows sufficient phase advance to be obtained while maintaining a smooth gain profile and avoiding excessive amplification at high frequencies (Fig.16).

Finally, the low-pass filter is included to attenuate high-frequency measurement noise and unmodeled dynamics, such as structural resonances and actuator limitations. This filtering action prevents noise amplification caused by the high-gain and phase-lead elements, thereby improving robustness and ensuring safe and reliable implementation of the controller.

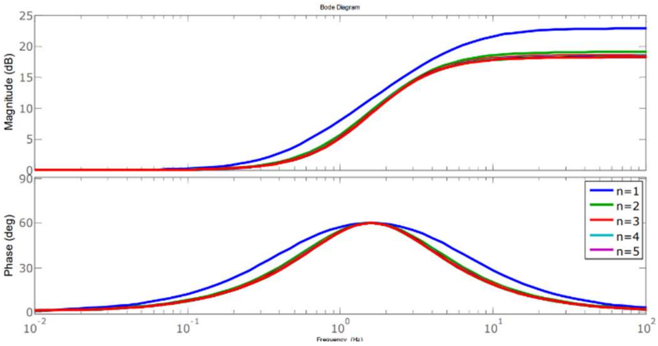

Figure 16 Orders of a phase-lead filter

Overall, this controller architecture naturally fits within a loop-shaping framework, where low-frequency gain is imposed for disturbance rejection, phase is shaped near the crossover frequency for stability, and high-frequency gain is reduced to preserve robustness.

The controller model for the conical mode is given as follows:

$$K_{con}(s) = \left(\frac{K_{Ic}}{s} + K_{Dc}\left(\frac{T_p + 1}{\alpha_D\, T_p\, s + 1}\right)^3 \frac{1}{\beta_D T_p s + 1}\right) F_{No}(s) \tag{26}$$

The controller model for the cylindrical mode is given as follows:

$$K_{cyl}(s) = \left(\frac{K_{Ic}}{s} + K_{Dc}\left(\frac{T_p + 1}{\alpha_D T_p\, s + 1}\right)^3 \frac{1}{\left(\frac{s^2}{{\omega_0}^2} + 2\frac{\xi}{{\omega_0}^2}\, s + 1\right)}\right) F_{No}(s) \tag{27}$$

The tuning of the cylindrical and conical controllers is based on the analysis of the rotor transfer function in the frequency domain. This transfer function provides essential insight into the rigid-body and flexible dynamics of the rotor and constitutes the basis for selecting the controller parameters.

The rotor transfer function can be obtained experimentally using a bump test, which allows the identification of both rigid and flexible modes by analyzing the system response to impulsive excitations (Fig.17). Such tests are commonly used to estimate resonance frequencies and damping characteristics required for control design. An experimental identification performed at 0 rpm can be used (Fig.18 & 19). Although this approach does not provide a parametric model of the rotor dynamics, it enables the measurement of the rotor frequency response to a series of controlled excitations over a defined frequency range. This non-parametric frequency response is sufficient to guide the loop-shaping process and to tune the gains and filters of the cylindrical and conical controllers, particularly with respect to bandwidth selection, phase margin, and resonance attenuation.

From the measured frequency response functions, the flexible modes of the rotor are observed in the frequency range between 150 Hz and 500 Hz (Fig.20 & 21). These modes correspond to structural resonances that may significantly affect closed-loop stability if not properly accounted for in the controller design. The frequency response also shows that the gain associated with the cylindrical modes exhibits significantly higher peaks than that of the conical modes. This indicates that the cylindrical dynamics are more sensitive to excitation in the flexible frequency range and therefore more prone to instability or excessive vibration amplification. A second-order low-pass filter is introduced in the cylindrical-mode controller. This filter effectively attenuates the contribution of high-frequency flexible modes, which are considered more critical for the cylindrical dynamics, while preserving the desired low-frequency control performance. In contrast, the lower gain levels observed in the conical modes allow a less restrictive filtering strategy.

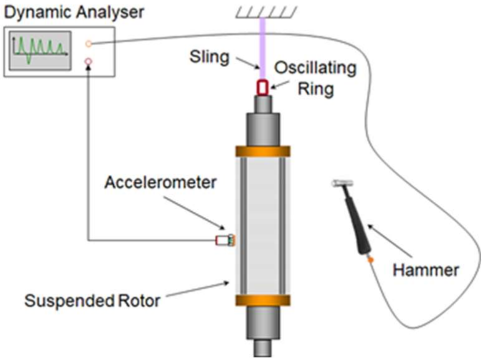

Figure 17 Rotor Bump Test

Figure 18 Testbench Modes Identification coupling side

Figure 19 Testbench Modes Identification opposite coupling side

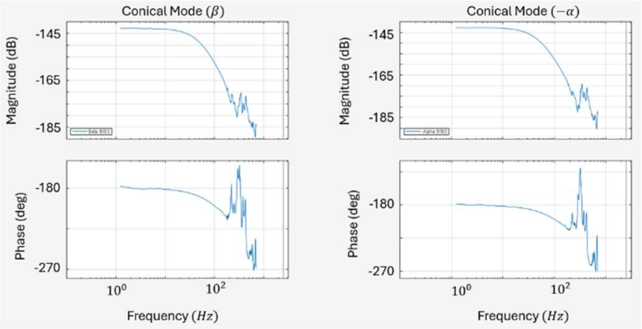

Figure 20 Rotor conical modes identification

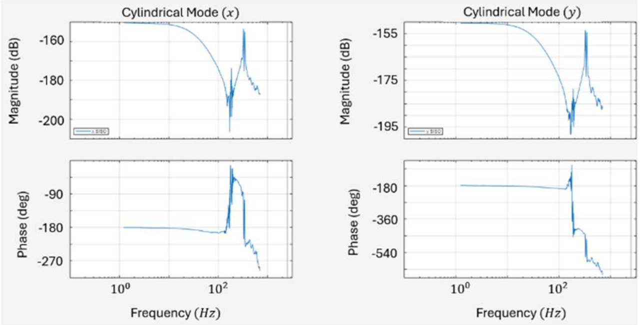

Figure 21 Rotor cylindrical modes identification

The analysis of the measured frequency response curves provides the necessary insight to synthesize the controller presented below. In particular, the location and amplitude of the rigid-body and flexible modes, as well as the differences observed between cylindrical and conical dynamics, directly guide the selection of the controller structure and parameters (Fig.22 & 23). The controller is implemented in discrete time with a sampling period of $T_s = 200e^{-0}\ s$. A continuous-time implementation is not feasible in practice, as the control algorithm is executed on a digital real-time platform. The use of digital sensors, analog-to-digital converters, and digital signal processing inherently imposes a sampled-data framework. Moreover, the presence of high-frequency flexible modes requires precise control of bandwidth and phase margins, which can only be consistently guaranteed when sampling effects, computational delays, and discretization are explicitly considered. Implementing the controller directly in continuous time and then discretizing it afterward could lead to performance degradation or instability due to unmodeled delays and aliasing effects. Based on this analysis, the following controller is constructed (Table II):

TABLE III
PARAMETERS OF THE TWO CONTROLERS

Conical	Cylindrical
K_{Ic} = 177 dB	K_{Ic} = 178 dB
K_{Dc} = 147 dB	K_{Dc} = 147 dB
T_p= 9.1e-03 s	T_p= 9.4e-04 s
$\alpha_{Dc} = 1.0599$	$\alpha_D = 1.0599$
$\beta_{Dc} = 0.4$	$\omega_0 = 1.26e+03$ rad/s
	$\xi = 0.4$

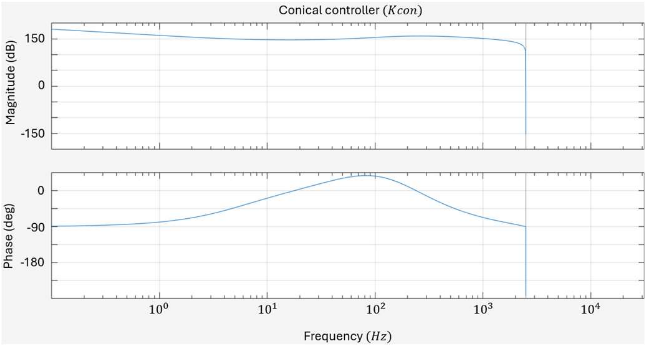

Figure 22 Conical Controller Discrete Bode

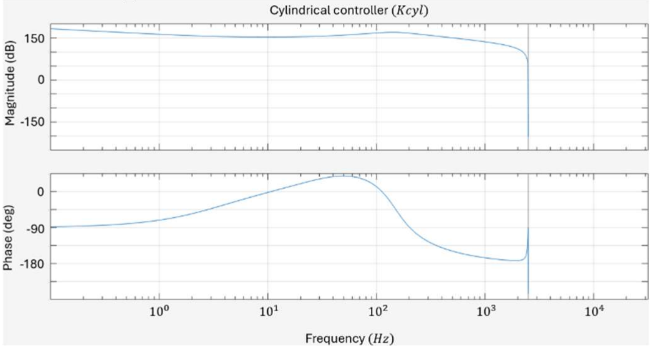

Figure 23 Cylindrical Controller Discrete Bode

The resulting controller is combined with the identified rotor dynamics to form the open-loop transfer function of the controlled system. Analyzing this open-loop behavior in the frequency domain, typically through Bode plots, makes it possible to verify that the control objectives are met. This analysis is used to assess the achieved gain and phase margins, to confirm closed-loop stability, and to ensure that the selected bandwidth and filter effectively balance performance and robustness (Fig.24 & 25).

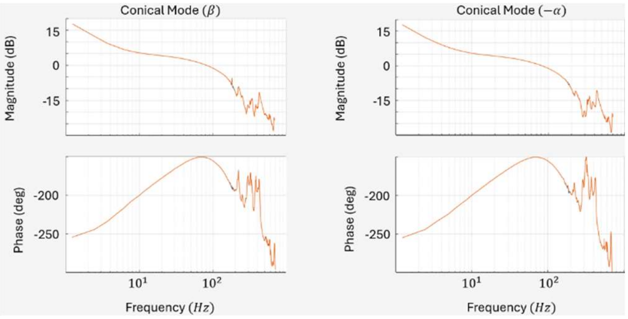

Figure 24 Conical System Open Loop transfer function

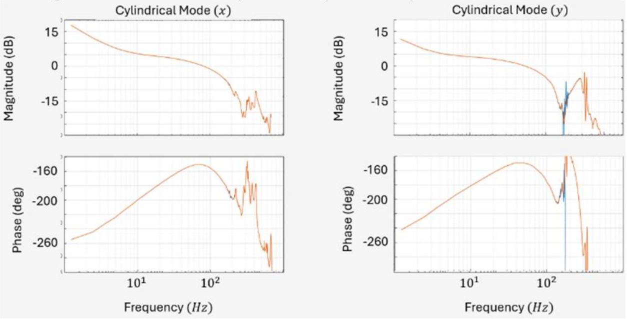

Figure 25 Cylindrical System Open Loop transfer function

Step changes in rotational speed are performed at several operating points (0 rpm, 4200 rpm, …, up to 11 000 rpm). At each speed step, an identification procedure identical to that used at 0 rpm is carried out. The purpose of this identification is to re-estimate the rotor dynamic behavior, since the rotor modes shift in frequency as the rotational speed increases due to gyroscopic effects and speed-dependent stiffness. The sensitivity is first analyzed in a SISO framework for each of the four controlled components, allowing individual assessment of performance and stability margins (Fig.26). A MIMO sensitivity analysis is then performed on the complete system to capture coupling effects between axes and modes and to ensure global closed-loop robustness over the entire speed range (Fig.26).

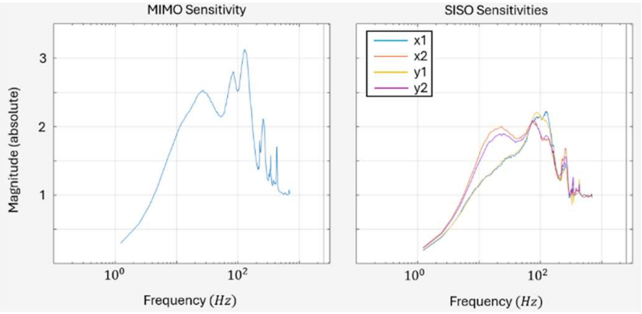

Figure 26 MIMO and four SISO cartesian sensitivities of the system

To further illustrate the effectiveness of the proposed control strategy, the following section presents the shaft centerline orbits obtained at different operating conditions 4200rpm (Fig.27 & 28) and 11000rpm (Fig.29 & 30). These results provide a direct time-domain visualization of the rotor dynamic behavior and the closed-loop performance [6].

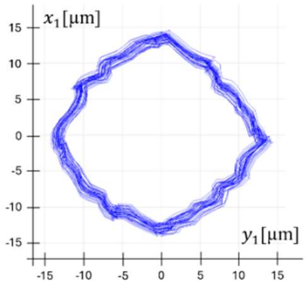

Figure 27 Tree Orbit x1 vs y1 4200rpm

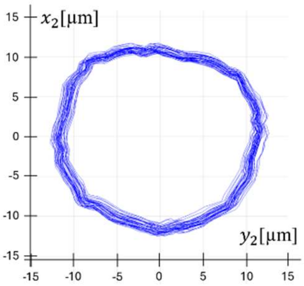

Figure 28 Tree Orbit x2 vs y2 4200rpm

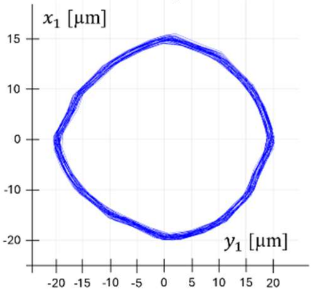

Figure 29 Tree Orbit x1 vs y1 11000rpm

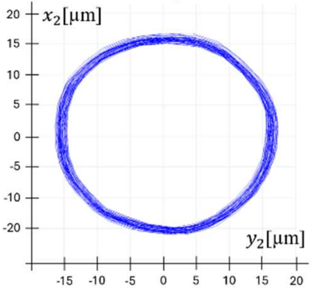

Figure 30 Tree Orbit x2 vs y2 11000rpm

III. CONCLUSION & PERSPECTIVES

The magnetic bearings are well-suited for a 7MW high-speed induction motor running at 15000 rpm. The chosen control system is robust. The power required to levitate the rotor is approximately 1kW. Currently with existing power amplifiers generating 4 kW and up to 6kW in peak transient conditions, it is possible to levitate rotors in rigid mode up to 10 tons spinning up to 7000 rpm. By scaling up the power of the existing technology of AMB, it will be possible to levitate rotors up to 100 tons with specific arrangements of axial thrust magnetic bearings [7].

A range of active magnetic bearings is under development that will enable the levitation of high-power rotors. A design is being finalized for an 80MW induction rotor rotating at 4200rpm with a mass of 24 tons. A cubicle incorporating 15kW power amplifiers will allow levitation and control of the rotor's position. Landing bearing suppliers can supply ceramic balls up to 40mm diameters required for the bearing diameters and rotor masses to be landed. There are no longer any technological limitations to using active magnetic bearings for very large, high-speed electrical machines.

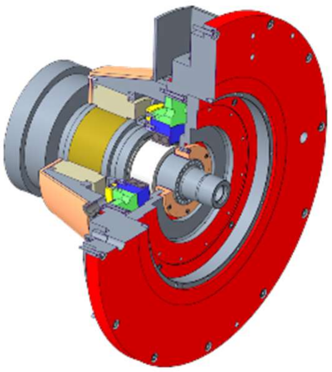

Figure 31 Active magnetic bearing standard platforming

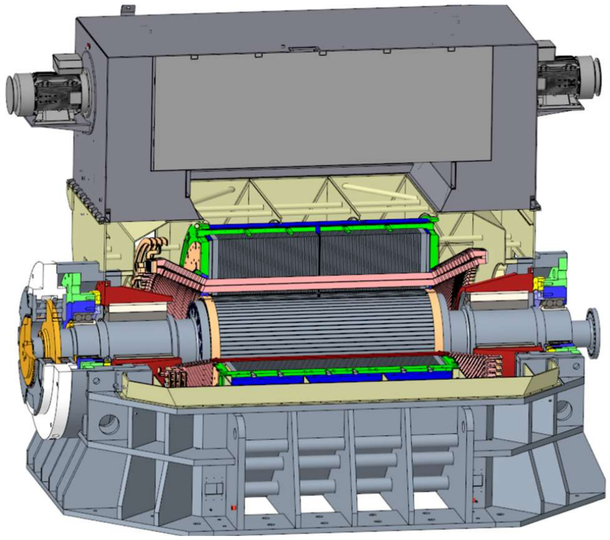

Figure 32 80MW@4200rpm Induction Motor
on Active Magnetic Bearings

IV. REFERENCES

[1]. J. West, G. Gallagher, “How they (should have) built the pyramids “, in American Physical Society Conference 2014, Denver, US, March 2014.

[2]. I. M. Hutchings, “Leonardo de Vinci’s Studies of Rolling-element, Disc and Sector Bearings”, *in Proc IMechE Part J: J Engineering Tribology,* Vol. 238(4) 372–389, 2024.

[3]. G. Schweitzer, E.H. Maslen, “Magnetic Bearings”, Springer Ed., Jan 2009, DOI: 10.1007/978-3-642-00497-1.

[4]. G. Mogenier, R. Dufour, G. Ferraris, L. Durantay, N. Barras, “Identification of Lamination Stack Properties: Application to High-speed Induction Motors”, *in IEEE Transactions on Industry Applications*, Vol. 57(1), Jan2010.

[5]. X. Delepine, Y. Lacour, “Set of Rolling Bearings and Corresponding Rotary Machine”, US Patent 9309922, April 12, 2016.

[6]. L. Durantay, C. Biri, A. Gelin, A. Kral, “Variable Speed Direct Drive Induction Motors Levitated by Active Magnetic Bearings for Oil&Gas Compression Services”, *in Proc of the 18th International Symposium on Magnetic Bearings,* ISMB18, Lyon, France, July 2023.

[7]. L. Durantay, E. Thibaut, A. Kral, M. Bouchakour, “Alternative Technology Trends and Returns of Experience of Compression Services Driven by Variable High-Speed Induction Motors Systems”, *in IEEE Transactions on Industry Applications,* Vol. 60(3) 5161–5173, May/June 2024.

V. NOMENCLATURE

σ_{mag}	Magnetic stress (Pa)	$F_X^{(k)}$	Pulling Force (N)
$I^{(k)}$	AMB coil current (A)	Area	Effective surface area (m²)
I_0	AMB Bias current (A)	B_{airgap}	Airgap Induction Field (T)
I_X	Current due to X (A)	μ_0	Vacuum permeability (H/m)
$g_X^{(k)}$	AMB airgap x axis (m).	α	Actuator polar angle (rad)
φ	Voltage-induced force phase (rad)	β	Current-induced force phase (rad)
N	# of Actuator turns	X	Displacement along X (m)
ω	Pulsation (rad/s)	L_a	Actuator Inductance (H)
Ω	Motor Speed (rad/s)	R_a	Actuator Resistance (Ω)
K_I	Electric Stiffness (N/A)	K_X	AMB Stiffness Amplitude (N/m)
$U_{piloted}$	Piloted voltage (V)	μ_r	Relative permeability (H/m)
K_{syst}	System Stiffness (N/m)	δ	Force component phase (rad)
τ	Phase delay (s)	D_s	Static Viscous Damping (Ns/m)
d	Actuator disturbance	D_r	Rotating Viscous Damping (Ns/m)
p	Output disturbance	C_{syst}	System Damping (Ns/m)
b	Sensor noise	h	Velocity Induced Voltage (V/m)
x_{ref}	Position reference (m)	g_0	Nominal air gap (m)
x	Position (m)	α_{con}	Conical mode angle (rad)
K_{Ic}	Integrator Gain (dB).	β_{con}	Conical mode angle (rad)
K_{Dc}	Phase-Lead Gain (dB)	x_{cyl}	Cylindrical mode in x (m)
T_p	Plant time constant (s)	y_{cyl}	Cylindrical mode in y (m)
ω_0	Filter pulsation (rad/s)	α_D	Derivative filter coefficient
ω_n	Notch pulsation (rad/s)	β_D	Derivative filter coefficient
ξ	Damping ratio	ξ_{No}	Notch damping ratio
UPS	Uninterruptible Power Supply battery		
AMB	Active Magnetic Bearing	CDS	Complex Dynamic Stiffness
SISO	Single Imput Single Output	MIMO	Multiple Input Multiple Output

VI. VITA

Lionel DURANTAY is graduated from the Ecole Nationale Supérieure d’Electricité et de Mécanique (ENSEM) in Nancy, France, with an engineering degree in 1989 then passed PhD in 1993. As R&D Leader, he has developed innovative variable speed electric systems for Oil & Gas, Air separation, onshore & offshore renewable, marine and navy businesses. He has authored or coauthored 58+ electromechanical papers, and supervised 6+ doctorates. He presently holds 30+ patents. He is 6-sigma Master Black Belt. He teaches statistical process control and design for 6-sigma at the University of Lorraine since 2005. He received GE's Thomas Edison Award in 2013 for technical excellence and customer impact. He is currently Chief Consulting Engineer & Global Product & Technology Leader within GE Vernova Power Conversion & Storage.

Jules MARULIER is student at the Ecole Nationale Supérieure d’Electricité et de Mécanique (ENSEM) in Nancy, France, preparing an engineering degree in electrical motors, power electronics & automation. He is currently intern at GE Vernova Power Conversion & Storage. In Q4’26, he will begin a three-year CIFRE PhD thesis on advanced variable speed electric motorization systems at GE Vernova Power Conversion & Storage.

Lionel BROUSSARD is graduated from Ecole Supérieure d’Electricité (ESE) in Gif sur Yvette, France, with an engineering degree, in 1988. He has over 35 years of experience in cold rolling mill control and he presently holds 2 patents and co-authored 1 paper in this field. He also works on the development of magnetic bearing control and co-authored 1 paper in this field. He is currently Senior Automation & Control Engineer at GE Vernova Power Conversion & Storage.

Christophe GROSSELIN is graduated from the Henri Loritz Lycée in 1987 and the ENIM of Metz, France (Ecole Nationale d’Ingénieurs de Metz) in 2002 with an engineering degree. He led several positions as product manager, customer support, engineering manager in France and in China. He has developed innovative motors and generators for Oil & Gas, air separation, onshore renewable, and navy businesses. He has coauthored 3+ papers. He presently holds 10+ patents. He received GE PC Innovation Award in 2022 for his contribution to high-speed technologies. He is currently Global Engineering Innovation & Platform Leader in GE Vernova Power Conversion & Storage.